JNeurosci
THE JOURNAL OF NEUROSCIENCE

Research Articles | Systems/Circuits

Cycle-by-cycle respiration waveforms are coupled with the shape of neural oscillations

https://doi.org/10.1523/JNEUROSCI.0731-26.2026

Received: 30 April 2026
Revised: 15 July 2026
Accepted: 6 August 2026

Title: Cycle-by-cycle respiration waveforms are coupled with the shape of neural oscillations

Abbreviated Title: Respiratory-neural waveform shape coupling

Eena Kosik-Rose[1*], Guangyu Zhou[5], Andrew Sheriff[5], Joshua M. Rosenow[6], Stephan U. Schuele[5], Chima O. Oluigbo[7,8], Saige Anabel Teti[7], Mohamad Koubeissi[8], Md Rakibul Mowla[9], Ariane E. Rhone[9], Sukhbinder Kumar[9], Brian Dlouhy[9†], Christina Zelano[5†], Bradley Voytek[1-4]

[1]Department of Cognitive Science, University of California, San Diego, La Jolla, CA, USA [2]Halıcıoğlu Data Science Institute, University of California, San Diego, La Jolla, CA, USA [3]Neurosciences Graduate Program, University of California, San Diego, La Jolla, CA, USA [4]Kavli Institute for Brain and Mind, University of California, San Diego, La Jolla, CA, USA, [5]Department of Neurology, Northwestern University Feinberg School of Medicine, Chicago, IL, USA, [6]Department of Neurosurgery, Northwestern University Feinberg School of Medicine, Chicago, IL, USA, [7]Department of Neurosurgery, Children's National Hospital, Washington, DC, USA, [8]Department of Neurology, George Washington University School of Medicine, Washington DC, USA, [9]Department of Neurosurgery, University of Iowa, Iowa City, IA, USA

[†]These authors contributed equally.

[*]**Corresponding author**: Eena Kosik-Rose, eena.kosik@gmail.com

Author contributions

E.K.R. and B.V.: Designed research. E.K.R.: Contributed unpublished reagents/analytic tools; Analyzed data; Wrote the first draft of the paper; Wrote the paper. B.V.: Wrote the paper. G.Z., A.S., J.M.R., S.U.S.,

C.O.O., S.A.T., M.K., M.R.M., A.E.R., S.K., C.Z., and B.D.: Performed research. All authors: Edited the paper.

Number of pages: 37

Number of figures: 5

Number of tables: 2

Word counts

Abstract: 187; Introduction: 650; Discussion: 1,489

Conflict of interest

The authors declare no competing financial interests.

Acknowledgements

This work was supported by the NIH National Institute of Mental Health grant R61MH135109. We are grateful to members of the Voytek Lab for their advice and feedback on the manuscript. The authors acknowledge the use of Claude (Anthropic) to assist with code optimization and language editing. No portion of the manuscript text was generated by AI; all scientific content, analyses, and interpretations are the authors' own.

Abstract

Beyond sustaining life, breathing is a vital physiological rhythm that shapes cognition, perception, emotional regulation, and mental health. Breathing has a direct effect on neuronal excitability and is coupled to neural oscillations across a variety of brain regions. Notably, both respiration and neural oscillations are asymmetric and not perfectly rhythmic: for example, every breath has a different shape and duration, and is interspersed with variable pauses. Here, we examined the coupling between breathing and the brain by quantifying the nonsinusoidal features of each breath and comparing it to the shape of each corresponding neural oscillation cycle. By leveraging invasive human brain recordings from 16 participants (8 female, 8 male), we found respiration-neural waveform coupling on a breath-by-breath, cycle-by-cycle basis across limbic and cortical forebrain regions. For decades, the dominant perspective on cognition and mental health have focused on the brain, but recent work is highlighting the importance of brain-body interactions. Our results show that the coupling between breathing and neural activity is much richer than previously appreciated, and our approach opens new avenues for studying these peripheral-to-central nervous system interactions in a more robust, temporally precise manner.

Significance Statement

Breathing shapes brain activity, but prior work has characterized this coupling by aggregating across many breath cycles, leaving the fine-grained shape of individual breaths unexamined. Here, we show that the precise waveform shape of each breath is coupled to the shape of corresponding neural oscillation cycles in the human forebrain, on a breath-by-breath basis. Using invasive brain recordings from 16 epilepsy patients, we demonstrate that temporal and amplitude features of individual breaths are linked to the morphology of neural oscillations in limbic and cortical regions. This cycle-by-cycle respiratory-neural coupling reveals a richer and more temporally precise relationship between breathing and brain activity than previously appreciated.

Introduction

Breathing is a vital rhythm of life, but recent work has revealed its role extends to higher-order cognitive and affective processes as well (Allen et al., 2023; Brændholt et al., 2023; Del Negro et al., 2018; Herrero et al., 2018; Kluger & Gross, 2021). While the mechanisms that relate respiration to these higher-order processes are less understood, neural responses to various external and internal stimuli have been shown to be dependent on the phase of respiration cycle (Brændholt et al., 2025; Harting et al., 2025; Mizuhara & Nittono, 2023; Park et al., 2020). Behaviorally, neural phase-dependence manifests across perceptual, memory, and emotion-related tasks, with performance peaking near the inhalation-exhalation transition (Arshamian et al., 2018; Grund et al., 2021; Johannknecht & Kayser, 2022; Kluger & Gross, 2020, 2021; Nakamura et al., 2022; Perl et al., 2019; Zelano et al., 2016).

One mechanistic hypothesis for this behavioral asymmetry is breathing's apparent influence on neural local field potentials (LFPs). Respiration can entrain LFPs in the mammalian forebrain, particularly in regions implicated in sensory, cognitive, and affective function (Herrero et al., 2018; Kluger & Gross, 2021; Zelano et al., 2016). Specifically, when the nasal pathway is bypassed, whether via tracheostomy in rats or mouth breathing in humans, respiration-locked brain rhythms disappear (Fontanini et al., 2003; Ito et al., 2014; Leupin & Britz, 2025; Zelano et al., 2016). However, emerging research has called this into question in humans, suggesting multiple afferent pathways for this neural synchronization, such as from the trachea, lungs, diaphragm, and chest wall (Mowla et al., 2026). Respiration even modulates single-unit membrane potential and spiking discharge in these non-olfactory regions (De Falco et al., 2024; Juventin et al., 2022; Karalis & Sirota, 2022).

Work assessing the relation between respiration and neural activity has been studied using a range of approaches, including phase-resolved analyses of neural responses, single-unit recordings, and magnitude-squared coherence (Tort, Brankačk, et al., 2018a; Tort et al., 2025; Tort, Ponsel, et al.,

2018b). While each is informative, these approaches share a common feature: they characterize coupling by aggregating across many breaths, whether by averaging cycles, binning by phase, or summarizing spectral relationships. As a result, they do not capture the fine-grained temporal coupling of individual respiratory and neural cycles. This is particularly important given the substantial variability in individual breath morphology – including asymmetries in rise and decay durations, differences in inhale peak volume, and inter-breath pauses – which can be masked using traditional approaches that assume respiration is a stable rhythm (Noto et al., 2018). This heterogeneity in oscillatory waveform shape has been clearly demonstrated in LFP signals, which have long been known to be asymmetric and bursty (Bender et al., 2025; S. R. Cole & Voytek, 2017; S. Cole & Voytek, 2019; Jones, 2016; Trimper et al., 2014). These nonsinusoidal features in the LFPs have been linked to a wide variety of cognitive and disease states (Trimper et al., 2014; S. R. Cole et al., 2017; Jackson et al., 2019). Whether respiration and neural oscillations are coupled not just in frequency, but in the fine-grained shape of each cycle, on a breath-by-breath basis, remains unknown.

In this study, we examine whether respiration and the neural LFP exhibit systematic, cycle-by-cycle alignment in waveform morphology. To do this, we introduce a novel, time-domain, cycle-resolved analysis that quantifies waveform shape features of both the respiration signal and LFP on a paired-cycle basis. We analyzed three human intracranial EEG (iEEG) datasets to quantify respiration waveform shape and its relationship to the shape of respiration-entrained neural oscillations across the forebrain at rest. We demonstrate that significant coherence between respiration and neural rhythms, while informative, does not inherently capture the cycle-by-cycle waveform dynamics between these signals. We provide, for the first time, strong evidence that the shape of every breath is coupled with the shape of the LFP on a breath-by-breath, cycle-by-cycle basis. Our results provide compelling evidence of respiration's fundamental role in modulating neural activity.

Materials and Methods

sEEG and respiration datasets

We analyzed previously collected data from three different recording locations. Sixteen participants with medically intractable epilepsy (10 participants from Northwestern Memorial Hospital, 3 participants from Children's National Hospital, and 3 participants from University of Iowa Stead Family Children's Hospital) underwent stereoelectroencephalography (sEEG) during a 2-week monitoring period for seizure focus localization. Participants' demographic data are shown in **Table 1**. All participants gave written informed consent and all methods were approved by the Institutional Review Board of the respective institutions. Participants and/or guardians could withdraw consent or assent at any point without affecting their clinical care. Electrode placement and respiratory monitoring techniques did not deviate from standard clinical procedures at each institution. All data ranged from 3.1 to 15.5 minutes. To assess whether this range affected the reliability of the current analysis, we examined the stability and reliability of coupling estimates across the range of session durations (see *Statistical analysis* below).

For participants at Northwestern Memorial Hospital and Children's National Hospital, the sampling rate, which was determined clinically, was 1,000 Hz or 2,000 Hz for all participants. A surgically implanted electrode strip facing towards the scalp or a surface electrode served as the reference and ground. Respiratory signals were recorded using a piezoelectric pressure transducer (Salter Labs BiNAPs 5500) attached to a nasal cannula placed at the participant's nose, and a breathing belt placed around the participant's abdomen (Perfect Fit II Adult Effort Belt, DyMedix Diagnostics). Participants were instructed to sit comfortably breathing through their noses with their eyes open while sEEG data were recorded using a clinical Nihon Kohden acquisition system with a built-in high-pass filter at 0.008 Hz. For participants at University of Iowa, they were implanted with intracranial electrodes (DIXI Medical US Products) at sites determined by the multidisciplinary epilepsy team. The sampling rate was 2000 Hz, and the filter setting at acquisition was 0.1 Hz to 500 Hz. A single subgaleal depth electrode was used as the reference. Respiratory signals were recorded using a piezoelectric pressure transducer (Salter Labs BiNAPs 5500) attached to a nasal cannula placed at the participant's nose, and a chest/abdominal

plethysmography belt (ProTech zRIP). Participants were instructed to rest quietly in the hospital bed while sEEG data were recorded to a Neuralynx ATLAS Neurophysiology System (Boseman, MT). Across all sites, 10 participants had respiration recordings from both modalities, 3 had only nasal cannula, and 3 had only breathing belt.

Data preprocessing

LFP and respiratory data were downsampled to 500 Hz using MNE in Python (version 3.11.10) (Gramfort, 2013). Recordings were bipolar re-referenced by subtracting the activity of adjacent electrode contact pairs to reduce noise, eliminate far-field effects, and decrease concerns over intracranial CSF pulsations and electrode movement synchronized to respiration. Respiratory signals were further low-pass filtered at 2 Hz using a finite impulse response (FIR) filter as implemented in MNE.

To determine the electrode locations for participants at Northwestern Memorial Hospital, the following procedure was used, as described in Zhou et al., 2021. The postoperative computed tomography images were registered to individual preoperative structural MRI images using FSL's linear registration tool (Jenkinson et al., 2002; Jenkinson & Smith, 2001). The transformed post-operative computed tomography images were thresholded and each electrode was identified manually. We used the center of each identified electrode as its coordinate in individual anatomical space. In order to visually represent electrodes across participants in one image, electrode coordinates were converted into MNI space by normalizing individual MRI images to a standard MNI brain (MNI152_1mm_brain) using FSL. We also performed subcortical segmentation of each individual's MRI image using FreeSurfer (Fischl, 2012; Fischl et al., 2002; RRID:SCR_001847).

For the participants at the Iowa Stead Family Children's Hospital, the following procedure was used, as described in Harmata et al., 2023. Whole-brain high-resolution T1-weighted structural MR scans (resolution and slice thickness ≤ 1.0 mm) were obtained before and after electrode implantation. Post-implantation CT and 3T MR structural scans were linearly coregistered to pre-implantation MR scans

using the FLIRT module of FSL (Jenkinson et al., 2002). These images were corrected manually for displacement and deformation from surgery using nonlinear thin-plate spline warping using manually selected control points. Finally, FreeSurfer was used to identify the cortical surface and white/gray boundaries within pre-implantation T1 images, which were corrected manually based on visual inspection where necessary.

Raw region labels, which varied in nomenclature across atlases and sites, were harmonized to a common set of anatomical categories using a custom label-normalization procedure applied uniformly across all participants. The atlas column in the electrode data frame records the source atlas for each participant. Electrode coverage by anatomical region for both the airflow and belt datasets is summarized in **Table 2**.

Coherence

To calculate coherence between the LFP and the breathing signals, we estimated cross-spectral and auto-spectral densities using the magnitude-squared coherence function implemented in 'scipy.signal.coherence' (Virtanen et al., 2020). Signals were segmented into epochs of 32 s with an overlap of 27 s following parameters from Herrero et al., (2018), where the 32 s window length provides a frequency resolution of 0.03 Hz (1/32 Hz), sufficient to capture the slow respiration rhythm. The magnitude-squared coherence was calculated as:

$$C(f) = \frac{|P_{xy}(f)|^2}{P_{xx}(f)P_{yy}(f)}$$

where

$$P_{xy}(f)$$

is the cross-spectral density and

$$P_{xx}(f), P_{yy}(f)$$

are the auto-spectral densities of the neural and respiratory signals, respectively.

For each neural channel, the maximum coherence value within each individual's breathing frequency range was extracted. This frequency range was determined by first computing the respiratory power spectral density (PSD) via Welch's method (Welch, 1967) using a 40 s Hanning window with a 20 s overlap. This long window is used to provide adequate frequency resolution (~0.025 Hz) to account for the slow respiration rhythm. Then, using the *specparam* toolbox (Donoghue et al., 2020), the center frequency of the highest amplitude peak was defined as the breathing frequency. A frequency band (0.2 Hz bandwidth) centered at the breathing frequency was used to bound the expected respiration-related frequency range in the coherence analysis.

To assess the statistical significance of coherence, we generated 1,000 surrogate neural signals for each LFP channel through phase randomization. To achieve this, LFP data were transformed to the frequency domain via Fast Fourier Transform (FFT), their phases were randomized while preserving amplitude spectra, and the LFPs were reconstructed in the time domain with inverse FFT. The coherence between each surrogate and the respective participant's respiratory signal was calculated, and a critical threshold was defined as the 99th percentile of surrogate coherence values. Coherence exceeding the threshold within the breathing frequency range was considered statistically significant ($p < 0.01$). Channels were retained for the next stage of analysis only if coherence at the respiration-frequency peak exceeded the

surrogate-derived threshold and the neural PSD had a *specparam*-identified peak within the same ± 0.1 Hz breathing frequency band. This dual criterion was applied based on the recommendation from Tort et al., (2025). It is possible that significant coherence and a local PSD peak can dissociate – a channel may show coherence without a local power peak or exhibit high coherence driven by harmonics of the breathing frequency without a fundamental peak due to the nonsinusoidal waveform morphology.

Cross-correlation analysis

Following the coherence-based selection of neural channels, we applied the first of two time-domain screening steps to ensure that the subsequent waveform shape analysis was appropriate: cross-correlations within fixed windows centered on the respiration peaks to provide consistent alignment across cycles.

First, neural and respiration signals were bandpass filtered between 0.01 and 2 Hz using a fifth-order Infinite Impulse Response (IIR) Bessel filter applied forward-backward (zero-phase) to preserve time-domain fidelity (Ghibaudo et al., 2023) and subsequently z-scored to normalize across time. Both signals were segmented into epochs centered on each respiration peak (corresponding to peak inhalation), with window lengths calibrated to each participant's breath cycle. Because windows were sized to the breath cycle, both the inhale peak and exhale trough were captured within each epoch.

Then, we computed the cross-correlation function (CCF) between the neural and respiration signals for each epoch, and then averaged CCFs across epochs yielding a mean CCF per channel, using `scipy.signal.correlate`. Lags were restricted to half of the respiration cycle to minimize spurious associations within a cyclical signal. From this restricted window, we extracted the maximum absolute value of the mean CCF for each LFP channel.

Statistical significance of the CCF was assessed using a permutation null distribution in which respiration epochs were paired with randomly sampled neural segments of equal length (drawn outside a 10 s margin around the original window). For each permutation (1000 iterations), a mean CCF was calculated from which the maximum absolute CCF value was extracted, yielding a channel-specific null distribution.

The significance threshold was defined as the 99th percentile of the null distribution ($p < 0.01$). Channel polarity was flipped at this stage when the mean CCF peak < 0 to account for arbitrary polarity from bipolar re-referencing.

Respiration phase monotonicity index

As a second time-domain screening step, we quantified whether the neural signals were consistently monotonic across the rising and falling phases of the respiration cycle using what we call a phase monotonicity index (PMI), adapted from the cycle-by-cycle analysis framework from S. Cole & Voytek, (2019).

Respiration cycles were first defined using troughs and peaks identified from the breathing signal. For each cycle, the corresponding neural signal was partitioned into a rising phase (trough to peak) and a falling phase (peak to subsequent trough). Within each phase, we computed the fraction of consecutive sample-to-sample differences that were directionally consistent with monotonic increase or decrease. A channel-level PMI value was obtained as the median PMI across all valid respiration cycles.

Statistical significance of the observed PMI was assessed using a circular-shift permutation null distribution. Neural signals were circularly shifted by a random offset of at least 10 s to disrupt their alignment with the respiration cycle while preserving temporal autocorrelation structure. For each permutation (1000 iterations), the PMI statistic was recomputed, yielding a null distribution against which the observed PMI was compared. The significance threshold was defined as the 99th percentile of the null distribution ($p < 0.01$), and channels were retained if the observed PMI exceeded the threshold.

Calculation of waveform shape features

Peak and trough detection

Peaks and troughs were extracted separately for neural and respiration signals using a two-stage adaptive procedure. In the first stage, candidate extrema were identified using `scipy.signal.find_peaks`, applying a base height threshold and a minimum inter-peak distance scaled to the sampling rate (distance = 1.5 × sampling frequency (fs)). A second pass refined detection by computing the median peak amplitude and applying a relative amplitude threshold. To ensure physiologically interpretable alternation between peaks and troughs, consecutive extrema of the same type were resolved by retaining only the more extreme point (higher peaks or deeper troughs). Cycles with abnormally large amplitude or root mean square (RMS; indicative of artifact or transient noise) were removed using robust median absolute deviation (MAD) thresholds.

Neural-respiration peak matching

To pair neural cycles with their corresponding respiratory cycles, we matched peaks in a one-to-one manner using a greedy nearest-neighbor procedure, which included iterating through each respiration peak in order and assigning it the temporally closest unmatched neural peak. The closest neural peak was accepted as a match if it was delayed less than one respiration period (τ), derived from the dominant respiration frequency. Peak pairs exceeding this threshold or lacking a following trough were excluded.

Cycle segmentation and waveform metrics

For each matched peak pair, cycle boundaries were defined using the nearest troughs immediately before and after each peak. Multiple waveform shape features were computed for both respiration and sEEG signals based on previous work (S. Cole & Voytek, 2019; Noto et al., 2018): rise time (onset trough time to peak time), decay time (peak time to subsequent trough time), cycle duration (sum of rise and decay times), amplitude (peak amplitude minus trough amplitude), sharpness (mean absolute first

derivative within a full-width-at-half-maximum (FWHM) window around inhale peaks and exhale troughs, normalized by local amplitude), area-under-the-curve (AUC; trapezoidal integration between median-crossing boundaries around inhale peak and exhale trough segments).

All resulting features were stored in a Pandas DataFrame (McKinney, 2010) containing one row per matched neural-respiration cycle.

To reduce the influence of extreme values, we applied feature-wise outlier exclusion. For each waveform metric (rise time, decay time, rise-decay symmetry, cycle duration, inhale peak/exhale trough sharpness and AUC), cycles exceeding 3 standard deviations above the median were discarded.

Experimental design and statistical analysis

This study used a within-subjects observational design. Sample size was determined by clinical availability of simultaneous iEEG and respiratory recordings; no a priori power analysis was conducted. Participants included 8 females and 8 males. Multiple comparisons were addressed through Bayesian inference and surrogate- and permutation-based null distributions rather than frequentist correction. This study was not preregistered.

To characterize the waveform shape features of both respiratory recording modalities, we compared airflow and belt features directly. For each feature, the median value across cycles was computed per participant, and paired differences between modalities were tested using the Wilcoxon signed-rank test across participants with valid recordings from both (N = 10). Because the two streams may differ systematically in their waveform properties, all subsequent analyses were conducted separately for airflow and belt.

Coherence and cross-correlation magnitude were compared between coupled and coherent-only (non-coupled) channels using two-sided Mann–Whitney U tests, with rank-biserial correlation as the effect size for airflow. The corresponding analysis was not done for belt due to the small number of belt-coupled channels (n=3).

Respiratory and neural waveform shape relationships were evaluated using Bayesian multilevel models fit in R v.4.5.2 (R Core Team, 2025) using the *brms* package v.2.23.0 (Bürkner, 2017). For each feature pair, neural features were modeled as a function of matched respiratory features using a within-between decomposition (Hamaker & Muthén, 2020; Mundlak, 1978). The respiratory predictor was split into within-subject and between-subject components, both scaled by their pooled standard deviations (SDs) to standardize coefficients comparable across features.

Compared to frequentist approaches, which determine whether there is an effect, Bayesian models output a probability distribution over the possible values of a parameter, called the posterior distribution. This enables direct probability statements about effect direction and magnitude rather than binary hypothesis testing (McElreath, 2020). Bayesian models were used because they provide stable estimates of complex random-effects structures and naturally accommodate the hierarchical nesting of participants and channels. We chose to use a Student's t likelihood, instead of a Gaussian, to accommodate any skewed data. Weakly informative priors were placed on all fixed effects ($\beta \sim \text{Normal}(0, 1)$), the intercept ($\text{Normal}(0, 2)$), variance components ($\text{Exponential}(1)$), and the degrees-of-freedom parameter ($\nu \sim \text{Gamma}(2, 0.1)$). The Markov chain Monte Carlo (MCMC) algorithm was applied with four chains of 3,000 iterations (1,500 warmup iterations) to obtain the posterior distribution for each parameter. Model adequacy was assessed via posterior predictive checks and convergence determined by the Rhat parameter (the ratio of the between to within chain variance) (Vasishth et al., 2018). For each model, the within-subject slope (β_{within}), its 95% credible interval (95% CrI), and the probability of β_{within} being greater than zero, $P(\beta > 0)$, are reported. Note that credible intervals (CrI) are a Bayesian quantity distinct from frequentist confidence intervals (CI): a 95% CrI directly expresses that, given the data and priors,

there is a 95% probability that the parameter lies within the stated range, which is not an interpretation available to frequentist CIs.

To assess whether observed coupling exceeded chance, we fit null models identical in structure to the primary models but using shuffled respiratory predictors. For each feature, the within-subject respiratory predictor (resp_within) was randomly permuted across cycles within each subject, disrupting cycle-by-cycle pairing while preserving the overall distribution of respiratory values and the multilevel structure of the data. Null models were fit using the same priors, sampler settings, and random effects structure as the primary models. Posterior distributions of β_within from null models are shown alongside those from real models in the corresponding results below; separation between real and null posteriors provides visual evidence of coupling beyond what would be expected under cycle-label randomization.

To evaluate whether session duration affected our results, we examined the relationship between session duration and coupling magnitude across participants, and additionally performed a split-half stability analysis on participants with above-median session duration, splitting each recording at its temporal midpoint and recomputing coherence and cross-correlation magnitude independently in each half.

Code accessibility

All analysis code used in this study is openly available at https://github.com/voytekresearch/ieeg_resp_shape. Scripts are written in Python and R.

Results

Respiration waveform shape is heterogeneous and can be rigorously quantified

We first quantified respiration waveform shape on a cycle-by-cycle basis using both nasal airflow and belt recordings (**Fig. 1a**). For each breath, we extracted rise time, decay time, total cycle duration, rise-decay

symmetry, inhale peak and exhale trough AUC, and inhale peak and exhale trough sharpness. These features captured the inherent asymmetry and diversity in shape of natural breathing.

Respiratory waveform morphology varied significantly across recording modalities (**Fig. 1b**; **Fig. S1**). To formally test modality differences, we compared within-subject airflow versus belt features using paired Wilcoxon signed-rank tests across participants who had both modalities collected (N = 10). These two modalities were significantly different in decay time (W = 8, p = 0.048), inhale peak AUC (W = 5, p = 0.019), exhale trough AUC (W = 3, p = 0.009), exhale trough sharpness (W = 0, p = 0.001), and inhale peak sharpness (W = 3, p = 0.009). In contrast, we didn't find any difference in rise time (W = 11, p = 0.105), rise-decay symmetry (W = 9, p = 0.064), and cycle duration (W = 14, p = 0.193). The fact that cycle duration did not differ between modalities implies that the airflow and belt yield comparable respiration rates despite systematic differences in waveform morphology. These results confirm that human respiration is nonsinusoidal – as evidenced by the asymmetry between rise and decay times and between inhale and exhale AUC – and exhibits rich, quantifiable morphology that varies meaningfully across cycles and modalities (Noto et al., 2018).

Respiration-neural coherence and waveform shape coupling identifies widespread respiration-locked activity

We next examined frequency-domain coupling between respiration and neural signals using magnitude-squared coherence within each participant's dominant breathing frequency band (**Fig. 2a–c**). However, visual inspection revealed that coherence alone did not necessarily imply clear cycle-by-cycle alignment in the time domain (**Fig. 2c**, middle row). Thus, two additional criteria were applied to ensure waveform-level correspondence: cross-correlation within respiration-centered windows and a respiration PMI. These criteria demonstrated that a subset of coherent channels exhibited coupling with consistent temporal lag structure (cross-correlation) and monotonic neural rise and fall aligned to the respiratory phases (PMI) (**Fig. 2c**).

Applying this coherence criterion, significant respiration-locked coherence (exceeding the 99th percentile of surrogate distributions) was observed in distributed cortical and limbic regions across airflow recordings (N = 13 participants; 1,459 channels total) and belt recordings (N = 13 participants; 1,361 channels total). Channels were retained only if: (i) coherence exceeded the 99th percentile of phase-randomized surrogates within ±0.1 Hz of the respiration peak frequency, and (ii) the neural power spectrum contained a corresponding periodic peak. This procedure identified 104 airflow-coherent channels across 13 participants and 109 belt-coherent channels across 13 participants (**Fig. 3a–b**, left panels).

Significant coherence with airflow was observed across distributed limbic and cortical regions (**Fig. 3a**, left). The two regions with the highest proportion of coherent channels, occipital cortex and transverse temporal cortex, were also the two most sparsely sampled regions in the dataset (**Table 2**); these proportions rest on very few electrodes and should be interpreted cautiously, and notably neither region contained any channels that survived subsequent waveform-shape screening (**Fig. 3a,** right). Among regions with broader coverage, the most prominent coherence was observed in inferior frontal gyrus, orbitofrontal cortex, insula, inferior and middle temporal cortex, with additional coherence observed in thalamus, hippocampus, and amygdala. Belt coherence showed a similarly distributed pattern (**Fig. 3b**, left), again led nominally by the sparsely sampled occipital cortex, with more robustly represented coupling in precentral gyrus, thalamus, middle temporal cortex, with additional contributions from inferior frontal gyrus, insula, hippocampus, and amygdala.

Although coherence was widespread, our criteria require waveform-level correspondence beyond frequency-domain coupling alone. Applying the cross-correlation and PMI criteria described above to all coherent channels, these sequential filters reduced the dataset to 16 airflow-coupled channels (across 7 participants), and 3 belt-coupled channels (across 3 participants) passing all screening criteria. Throughout, we refer to channels passing the coherence screen as "coherent" and reserve "coupled" for

channels passing all three screening criteria (coherence, cross-correlation, and PMI), which form the basis for all cycle-by-cycle waveform shape analyses. In total, these analyses draw on 7 of the 16 participants. Representative time series, coherence spectra, and time-frequency coherence plots for example airflow- and belt-coupled channels are shown in **Fig. S2**.

Among airflow-coupled channels, waveform shape modulation was concentrated in a smaller subset of regions (**Fig. 3a**, right), with channels in inferior frontal gyrus, caudal middle frontal and superior frontal gyrus, insula, as well as single channels in orbitofrontal cortex, middle temporal cortex, hippocampus, thalamus, and fusiform cortex. In contrast, waveform shape modulation for belt signals was substantially sparser (**Fig. 3b**, right), with single channels in the amygdala, orbitofrontal cortex, and middle temporal cortex. Among airflow-coupled channels passing all waveform shape criteria, two channels localized to white matter. While these channels passed all screening criteria, white matter channels are not expected to reflect local neural generators and likely reflect volume conduction from adjacent gray matter sources.

Region-level overlap between airflow and belt coupling was quantified using Dice similarity coefficients (a region counted as positive if ≥1 channel passed the criterion). Overlap was near-complete for coherence (Dice = 0.947) but substantially lower for waveform-shape coupling (Dice = 0.308); the latter should be interpreted cautiously given the small number of belt-coupled channels.

We next asked whether the strength of coherence itself predicts which channels go on to show waveform coupling, comparing coherence and cross-correlation magnitude between airflow channels that passed full waveform screening (coupled; n = 16) and those that exhibited significant coherence but did not pass time-domain screening (coherent-only; n = 88). Coupled channels exhibited higher coherence magnitude (median 0.75, IQR [0.62, 0.87] vs 0.32, IQR [0.21, 0.49]; Mann-Whitney U = 1160.5, $p < 0.001$, rank-biserial r = 0.61) and higher peak cross-correlation magnitude (median 0.48, IQR [0.35, 0.66] vs 0.09, IQR [0.06, 0.15]; U = 1237.0, $p < 0.001$, r = 0.72) (**Fig. S3**). Thus, channels exhibiting cycle-by-cycle

waveform coupling tended to be those with the strongest global coupling. Notably, however, strong coherence was not sufficient for waveform coupling: the 16 coupled channels represented a small fraction of channels with significant coherence, indicating that high coherence raises the likelihood of, but does not guarantee, cycle-by-cycle waveform coupling. The corresponding analysis was not done for belt channels due to the small number of channels that were significantly waveform coupled (n=3).

Recording durations ranged from 3.1 to 15.5 minutes. Participants and channels contributing significant airflow and belt waveform-shape coupling spanned nearly the full duration range (3.1–15.3 minutes) (**Fig. S4a**). Coupling magnitude did not decrease with shorter sessions; if anything, coherence and cross-correlation magnitude correlated negatively with duration (coherence: airflow $r = -0.86$, belt $r = -0.86$, both $p < .001$; cross-correlation: airflow $r = -0.55$, $p = .051$, belt $r = -0.55$, $p = .053$), indicating that shorter recordings were not underpowered relative to longer ones (**Fig. S4b**). A split-half stability analysis (participants with above-median duration; airflow $n = 7$, belt $n = 7$) showed strong agreement between first- and second-half estimates for both cross-correlation (airflow $r = 0.84$, belt $r = 0.85$) and coherence (airflow $r = 0.67$, belt $r = 0.80$, all $p < .0001$) (**Fig. S4c**). Together, these analyses indicate that the range of recording durations does not compromise the reliability of our coupling estimates.

Respiratory waveform shape is coupled to neural waveform shape

We next asked whether cycle-by-cycle variation in respiration morphology relates to neural oscillation morphology. Using Bayesian linear mixed-effects models, neural waveform features were modeled as a function of matched respiratory features using a within-between decomposition. All features were scaled by their pooled (grand) standard deviation prior to modeling, such that standardized slopes (β) reflect within-subject coupling strength and are directly comparable across features.

Airflow waveform features showed consistent positive relationships with corresponding neural waveform features (**Fig. 4a–b**): Cycle duration: β = 0.24 [0.07, 0.44], P(β > 0) = 1.00; Peak AUC: β = 0.19 [0.10, 0.30], P(β > 0) = 1.00; Decay time: β = 0.16 [0.06, 0.26], P(β > 0) = 1.00; Trough AUC: β = 0.15 [0.03, 0.28], P(β > 0) = 0.99; Rise time: β = 0.20 [−0.02, 0.43], P(β > 0) = 0.97; Trough sharpness: β = 0.06 [−0.01, 0.13], P(β > 0) = 0.96; Rise-decay symmetry: β = 0.13 [−0.06, 0.33], P(β > 0) = 0.91; Peak sharpness: β = −0.02 [−0.09, 0.04], P(β > 0) = 0.23. Comparison against null models fit on cycle-shuffled data showed that the two area-under-the-curve features most clearly separated from the null (peak AUC, P(real > null) = 0.99; trough AUC, P = 0.98), while the remaining features showed directional posterior slopes that overlapped more substantially with the cycle-shuffled null (**Fig. 4a**). These results indicate positive coupling between airflow and neural waveform morphology, most robustly for amplitude (AUC) features.

Belt-derived results showed no directional coupling for any waveform feature, with all posterior slopes spanning zero and P(β > 0) near chance: Rise time: β = 0.03 [−0.47, 0.53], P(β > 0) = 0.57; Decay time: β = −0.10 [−0.80, 0.52], P(β > 0) = 0.37; Cycle duration: β = 0.11 [−0.47, 0.67], P(β > 0) = 0.73; Rise-decay symmetry: β = −0.07 [−0.54, 0.39], P(β > 0) = 0.33; Peak sharpness: β = −0.04 [−0.51, 0.50], P(β > 0) = 0.36; Trough sharpness: β = 0.02 [−0.41, 0.42], P(β > 0) = 0.57; Peak AUC: β = 0.23 [−0.48, 0.91], P(β > 0) = 0.81; Trough AUC: β = −0.04 [−0.29, 0.22], P(β > 0) = 0.31. We note that with only 3 belt-coupled channels these models are underpowered: several models exhibited divergent transitions (up to 111 for rise-decay symmetry), indicating the sampler could not reliably explore the posterior. Belt results are therefore reported for completeness only and we make no inferential claims from them. Correspondingly, belt model posteriors overlapped the null model posteriors across all features (**Fig. 4a**). Thus, while airflow features showed evidence for coupling with neural waveform morphology, belt signals did not.

The cycle-by-cycle scatter plots illustrate this pattern visually: airflow regression lines show mostly consistent positive slopes across channels for temporal features (rise time, decay time, cycle duration) and amplitude features (inhale peak and exhale trough AUC), whereas belt regression lines are variable

in direction, and peak sharpness slopes are flat in both modalities, while trough sharpness shows a modest positive slope for airflow (**Fig. 5**). See **Fig. S4** for visualizing the raw time series of exemplar waveform-coupled channels for airflow and belt.

Discussion

Across three independent human sEEG datasets, we confirm widespread respiratory-neural coherence across limbic and cortical regions. Among coherent channels, a subset also exhibit morphological coupling such that respiratory waveform shape is related to neural oscillation waveform shape on a cycle-by-cycle basis, an effect substantially stronger for nasal airflow than belt recordings.

Humans breathe in asymmetric, nonsinusoidal shapes, with varying inhalation and exhalation durations, pauses between breaths, and differences in the volume/intensity of air that gets inhaled and exhaled. Prior work has demonstrated that there are rhythms in the brain that are statistically coherent with breathing (Tort et al., 2025); however, this metric averages over cycle-level variability and doesn't imply that the neural oscillations are systematically synchronized with the precise waveform shapes of the respiration. We therefore isolated neural channels with waveform coupling to both airflow and belt waveforms, matched these signals on a cycle-by-cycle basis, parameterized their waveform shapes, and found that respiration shape is reliably related to neural shape in expected regions.

This relationship suggests that respiration may modulate the shapes of neural waveforms in a temporally-precise manner. Neural oscillation waveform shape is thought to represent properties of the underlying physiological generators of the LFP, including the synchrony of various postsynaptic potentials and the timing of population-level firing (S. R. Cole & Voytek, 2017; Trimper et al., 2014). If respiration shapes the waveform morphology of neural oscillations on a cycle-by-cycle basis, as we demonstrate here, this implies that breath-to-breath variation may directly modulate the temporal structure of neural activity in limbic and

cortical regions. In other words, the asymmetry of the breath cycle – how quickly or slowly air flows in and out – may impact the time windows available for spike probability and inter-regional communication (Karalis & Sirota, 2022). This is consistent with, and may help explain, single-unit evidence that human thalamic neurons themselves preferentially spike during inhalation versus exhalation (De Falco et al., 2024): if breath asymmetry shapes the timing windows available for spiking, this offers a candidate mechanism for why individual neurons show phase-locked firing to respiration. Our findings extend this mechanistic chain further, from spike timing and state duration to the shape of the aggregate LFP waveform, suggesting that the continuous morphology of each breath, not just inhale versus exhale, is reflected in ongoing neural dynamics. By volitionally altering the time spent in different respiratory phases, thereby manipulating the respiration shape, individuals may systematically change the windows available for spike generation, synaptic integration, and communication between brain regions. This may help explain why deliberate breathing practices that emphasize different respiratory phase durations can produce distinct affective effects (Balban et al., 2023), and why natural, stimulus-driven changes in breath timing likewise track shifts in emotional state (Vlemincx et al., 2015).

The substantially stronger coupling observed for nasal airflow compared to the respiratory belt is consistent with the interpretation that the underlying driver of this effect arises from the nasal airflow pathway and its early projections into limbic circuitry rather than from the mechanical act of breathing itself (Fontanini et al., 2003; Juventin et al., 2022; Lockmann et al., 2016; Zelano et al., 2016). However, recent work has demonstrated that forebrain synchronization with breathing in humans persists even when airflow bypasses the oronasal passages entirely (Mowla et al., 2026). The weaker coupling from the belt could therefore reflect not the absence of a mechanistic link, but rather the limited fidelity of the belt as a recording instrument, which coarsely measures chest wall displacement rather than nasal airflow dynamics directly (Johnson et al., 2006). Nasal airflow recordings preserve certain temporal features of the breath cycle that the belt signal misses, such as the post-expiratory pause (PEP). This waveform feature carries functional significance for limbic circuits and predicts depression and life satisfaction (Diez et al., 2025). The richness of the nasal airflow signal even extends towards stable, distinctive respiratory

507 “fingerprints” that track with physiological and behavioral states (Soroka et al., 2025), underscoring that
508 airflow shape is not incidental, but carries systematic, individually meaningful information.

509

510 The regional distribution of waveform-coupled channels is broadly consistent with known anatomy of
511 respiration-brain pathways. Airflow-coupled channels were distributed across frontal, limbic, and temporal
512 regions, with the highest proportions in lateral and middle frontal cortex (caudal middle frontal and
513 superior frontal gyri) and additional coupling in inferior frontal gyrus, insula, orbitofrontal cortex,
514 hippocampus, thalamus, fusiform, and middle temporal gyrus (**Fig. 3a, right**). Belt-coupled channels were
515 sparser still and confined to amygdala, orbitofrontal cortex, and middle temporal gyrus (**Fig. 3b, right**). A
516 direct anatomical pathway links nasal airflow to limbic and cortical regions: mechanoreceptors in the
517 nasal epithelium project via the olfactory bulb to piriform cortex and from there to the amygdala,
518 hippocampus, and insula, providing a substrate for airflow-specific entrainment of forebrain activity
519 (Fontanini et al., 2003; Juventin et al., 2022; Zelano et al., 2016). The insula is known to be strongly
520 synchronized to breathing, particularly anterior insula (Assi et al., 2025; Mowla et al., 2026) due to its role
521 as an interoceptive hub integrating ascending visceral signals to predict bodily states ((Bud) Craig, 2009;
522 Chen et al., 2021; Khalsa et al., 2009). Temporal and frontal regions are likewise consistent with broad
523 forebrain distribution of respiration-coherent channels during wakefulness (Mowla et al., 2026) and
524 resting-state fMRI work has specifically shown that nasal – but not oral – breathing promotes functional
525 connectivity between olfactory regions and lateral frontal cortex including IFG, consistent with our finding
526 that IFG waveform coupling was observed for airflow but not belt signals (Mohammadi et al., 2025).
527 Furthermore, the concentration of waveform-coupled channels in insula-adjacent limbic and cortical
528 regions is consistent with their role as core nodes of the salience network, which integrates interoceptive
529 and affective signals, and is linked to precise temporal features of airflow (Diez et al., 2025). Additionally,
530 recent work has demonstrated that thalamus is an important region for respiratory information; single-unit
531 recordings in human thalamus were shown to actively encode the temporal structure and phases of the
532 breath, preferentially spiking during inhalation versus exhalation (De Falco et al., 2024). Finally, two
533 airflow-coupled channels were localized to white matter, which is unlikely to reflect local synaptic activity

and most plausibly arises via volume conduction from nearby gray matter sources (Herrero et al., 2018). Notably, the overwhelming concentration of waveform-coupled channels in gray matter and the relative rarity of white matter channels is itself consistent with the interpretation that the observed coupling reflects genuine neural activity rather than a respiratory mechanical artifact.

There are a number of limitations to the present study. Our method isolated only a small number of channels exhibiting significant waveform shape coupling, particularly for belt recordings, reflecting the difficulty of detecting this signal even when coherence is present. Notably, only three channels across three participants passed all screening criteria for belt-based waveform shape analysis, making the belt models severely underpowered and their null results difficult to interpret in isolation. That said, the fact that belt channels were disproportionately filtered out by the time-domain screening steps, despite comparable numbers of coherent channels, is itself informative, even if the statistical models were underpowered. Additionally, all participants were epilepsy patients undergoing invasive monitoring, with electrode placement determined by clinical need rather than experimental design. The underlying pathology, antiseizure drug regimens, and uneven cortical and subcortical coverage across participants may limit generalizability to healthy populations (see **Table 1** for information on participants). While these limitations are inherent to this modality, our findings complement non-invasive work on respiration-brain coupling (Kluger and Gross, 2021; Pfurtscheller et al., 2023; Watanabe et al., 2023). Because fMRI offers spatial but not temporal precision, and EEG/MEG offer temporal precision but rely on source reconstruction, our intracranial recordings instead provide ground-truth electrical activity at known anatomical locations, with the precision cycle-by-cycle analysis requires. These findings raise the possibility of extending this cycle-by-cycle analysis to non-invasive modalities.

Future research should also leverage volitional breath control (e.g., manipulating breath route, depth, or shape) to determine whether controlling respiratory waveform shape influences the shape of neural waveforms in a causal manner. This is a particularly promising direction given evidence that oral and nasal respiration modulate sensory and cognitive brain potentials differently (Leupin & Britz, 2025),

suggesting that breath route plays an active role in neural processing. Unlike passive breathing at rest, volitional breathing recruits frontal, motor, and premotor circuits (Herrero et al., 2018), introducing a top-down component to the respiration-brain pathway. If deliberate manipulation of breath shape drives corresponding changes in the neural waveform, this would suggest a bidirectional pathway in which frontal control of breathing feeds back onto the limbic and cortical dynamics that breathing entrains. Beyond controlled manipulations of breathing, future work could determine whether respiratory waveform shape features – not just respiratory phase – predict trial-by-trial variability during cognitive, affective, or perceptual tasks, potentially incorporating other markers of brain state (e.g., alpha power (Chalas et al., 2026)) and more direct measures of respiratory effort (e.g., EMG). This would help establish whether the cycle-by-cycle morphological coupling we demonstrate here has direct behavioral implications.

References

Allen M, Varga S, Heck DH (2023) Respiratory rhythms of the predictive mind. Psychol Rev 130:1066–1080.

Arshamian A, Iravani B, Majid A, Lundström JN (2018) Respiration modulates olfactory memory consolidation in humans. J Neurosci 38:10286–10294.

Assi JY, Bickel S, Greenberg HE, Mehta AD, Similowski T, Herrero JL (2025) Insular routing to orbitofrontal cortex enables breathing awareness. medRxiv. doi:10.1101/2025.08.28.25334357.

Balban MY, Neri E, Kogon MM, Weed L, Nouriani B, Jo B, Holl G, Zeitzer JM, Spiegel D, Huberman AD (2023) Brief structured respiration practices enhance mood and reduce physiological arousal. Cell Rep Med 4:100895.

Bender A, Voytek B, Schaworonkow N (2025) Resting-state alpha and mu rhythms change shape across development. J Cogn Neurosci 37:1581–1615.

583 Brændholt M, Kluger DS, Varga S, Heck DH, Gross J, Allen MG (2023) Breathing in waves:
584 understanding respiratory-brain coupling as a gradient of predictive oscillations. Neurosci
585 Biobehav Rev 152:105262.

586 Brændholt M, Nikolova N, Vejlø M, Banellis L, Fardo F, Kluger DS, Allen M (2025) The respiratory cycle
587 modulates distinct dynamics of affective and perceptual decision-making. PLoS Comput Biol
588 21:e1013086.

589 Bürkner PC (2017) brms: an R package for Bayesian multilevel models using Stan. J Stat Softw 80:1–28.

590 Chalas N, Saltafossi M, Berther T, Balestrieri E, Abbasi O, Kluger DS (2026) Respiration as a dynamic
591 modulator of sensory sampling. Nat Commun 17:3261

592 Chen WG, Schloesser D, Arensdorf AM, Simmons JM, Cui C, Valentino R, Gnadt JW, Nielsen L, Hillaire-
593 Clarke CS, Spruance V, Horowitz TS, Vallejo YF, Langevin HM (2021) The emerging science of
594 interoception. Trends Neurosci 44:3–16.

595 Cole S, Voytek B (2019) Cycle-by-cycle analysis of neural oscillations. J Neurophysiol 122:849–861.

596 Cole SR, van der Meij R, Peterson EJ, de Hemptinne C, Starr PA, Voytek B (2017) Nonsinusoidal beta
597 oscillations reflect cortical pathophysiology in Parkinson's disease. J Neurosci 37:4830–4840.

598 Cole SR, Voytek B (2017) Brain oscillations and the importance of waveform shape. Trends Cogn Sci
599 21:137–149.

600 Craig ADB (2009) How do you feel — now? The anterior insula and human awareness. Nat Rev Neurosci
601 10:59–70.

602 De Falco E, Solcà M, Bernasconi F, Babo-Rebelo M, Young N, Sammartino F, Tallon-Baudry C, Navarro
603 V, Rezai AR, Krishna V, Blanke O (2024) Single neurons in the thalamus and subthalamic nucleus
604 process cardiac and respiratory signals in humans. Proc Natl Acad Sci USA 121:e2316365121.

Del Negro CA, Funk GD, Feldman JL (2018) Breathing matters. Nat Rev Neurosci 19:351–367.

Diez GG, Cuesta P, Lazar SW, Saracho L, Bruña R, Maestú F, Anitua E, Castellanos N (2025) Unmasking the post-expiratory pause. Cereb Cortex 35:bhaf313.

Donoghue T, Haller M, Peterson EJ, Varma P, Sebastian P, Gao R, Noto T, Lara AH, Wallis JD, Knight RT, Shestyuk A, Voytek B (2020) Parameterizing neural power spectra into periodic and aperiodic components. Nat Neurosci 23:1535–1544.

Fischl B (2012) FreeSurfer. NeuroImage 62:774–781.

Fischl B, Salat DH, Busa E, Albert M, Dieterich M, Haselgrove C, van der Kouwe A, Killiany R, Kennedy D, Klaveness S, Montillo A, Makris N, Rosen B, Dale AM (2002) Whole brain segmentation. Neuron 33:341–355.

Fontanini A, Spano P, Bower JM (2003) Ketamine-xylazine-induced slow oscillations in the rat piriform cortex are functionally correlated with respiration. J Neurosci 23:7993–8001.

Ghibaudo V, Granget J, Dereli M, Buonviso N, Garcia S (2023) A unifying method to study respiratory sinus arrhythmia dynamics. eNeuro 10:ENEURO.0197-23.2023.

Gramfort A (2013) MEG and EEG data analysis with MNE-Python. Front Neurosci 7:267.

Grund M, Al E, Pabst M, Dabbagh A, Stephani T, Nierhaus T, Gaebler M, Villringer A (2021) Respiration, heartbeat, and conscious tactile perception. J Neurosci 41:7988–8002.

Hamaker EL, Muthén B (2020) The fixed versus random effects debate and how it relates to centering in multilevel modeling. Psychol Methods 25:365–379.

Harmata GIS, Rhone AE, Kovach CK, Kumar S, Mowla MR, Sainju RK, Nagahama Y, Oya H, Gehlbach BK, Ciliberto MA, Mueller RN, Kawasaki H, Pattinson KTS, Simonyan K, Davenport PW, Hockman

MA, Steinschneider M, Chan AC, Richerson GB, Dlouhy BJ (2023) Failure to breathe persists without air hunger or alarm following amygdala seizures. JCI Insight 8:e172423.

Harting C, Hehemann L, Stetza L, Kayser C (2025) Respiration shapes response speed and accuracy with a systematic time lag. Proc R Soc B 292:20242566.

Herrero JL, Khuvis S, Yeagle E, Cerf M, Mehta AD (2018) Breathing above the brain stem: volitional control and attentional modulation in humans. J Neurophysiol 119:145–159.

Ito J, Roy S, Liu Y, Cao Y, Fletcher M, Lu L, Boughter JD, Grün S, Heck DH (2014) Whisker barrel cortex delta oscillations and gamma power in the awake mouse are linked to respiration. Nat Commun 5:3572.

Jackson N, Cole SR, Voytek B, Swann NC (2019) Characteristics of waveform shape in Parkinson's disease detected with scalp electroencephalography. eNeuro 6:ENEURO.0151-19.2019.

Jenkinson M, Bannister P, Brady M, Smith S (2002) Improved optimization for robust and accurate linear registration of brain images. NeuroImage 17:825–841.

Jenkinson M, Smith S (2001) A global optimisation method for robust affine registration of brain images. Med Image Anal 5:143–156.

Johannknecht M, Kayser C (2022) The influence of the respiratory cycle on reaction times in sensory-cognitive paradigms. Sci Rep 12:2505.

Johnson BN, Russell C, Khan RM, Sobel N (2006) A comparison of methods for sniff measurement concurrent with olfactory tasks in humans. Chem Senses 31:795–806.

Jones SR (2016) When brain rhythms aren't 'rhythmic': implication for their mechanisms and meaning. Curr Opin Neurobiol 40:72–80.

Juventin M, Ghibaudo V, Granget J, Amat C, Courtiol E, Buonviso N (2022) Respiratory influence on brain dynamics: the preponderant role of the nasal pathway. Pflugers Arch 474:827–840.

Karalis N, Sirota A (2022) Breathing coordinates cortico-hippocampal dynamics in mice during offline states. Nat Commun 13:467.

Khalsa SS, Rudrauf D, Feinstein JS, Tranel D (2009) The pathways of interoceptive awareness. Nat Neurosci 12:1494–1496.

Kluger DS, Gross J (2020) Depth and phase of respiration modulate cortico-muscular communication. NeuroImage 222:117272.

Kluger DS, Gross J (2021) Respiration modulates oscillatory neural network activity at rest. PLoS Biol 19:e3001457.

Leupin V, Britz J (2025) Oral respiration modulates sensory and cognitive brain potentials differently than nasal respiration. Sci Rep 15:29401.

Lockmann ALV, Laplagne DA, Leão RN, Tort ABL (2016) A respiration-coupled rhythm in the rat hippocampus independent of theta and slow oscillations. J Neurosci 36:5338–5352.

McElreath R (2020) Statistical rethinking: a Bayesian course with examples in R and Stan, 2nd ed. Boca Raton, FL: Chapman and Hall/CRC.

McKinney W (2010) Data structures for statistical computing in Python. In: Proceedings of the 9th Python in Science Conference, pp 56–61.

Mizuhara K, Nittono H (2023) Effects of respiratory phases on the processing of emotional and non-emotional visual stimuli. Psychophysiology 60:e14261.

Mohammadi S, Hossein-Zadeh GA, Raoufy MR (2025) Breathing mode selectively modulates brain-wide functional connectivity. PLoS One 20:e0334165.

669 Mowla MR, Rhone AE, Kumar S, Kovach CK, Liu JV, Chan AC, Kawasaki H, Mueller RN, Kuhn JD, Frede
670 RT, Ciliberto MA, Czech TM, Thati Ganganna S, Owens JW, Dabrowski AK, Sprigg BN, Granner
671 MA, Simonyan K, Nourski KV, Krause BM, Banks MI, Howard MA 3rd, Davenport PW, Pattinson
672 KTS, Richerson GB, Wemmie JA, Dlouhy BJ (2026) Human forebrain neural synchronization and
673 entrainment to breathing during wakefulness, sleep, and external mechanical ventilation. Nat
674 Commun. Advance online publication. doi:10.1038/s41467-026-73828-0.

675 Mundlak Y (1978) On the pooling of time series and cross section data. Econometrica 46:69–85.

676 Nakamura NH, Fukunaga M, Yamamoto T, Sadato N, Oku Y (2022) Respiration-timing-dependent
677 changes in activation of neural substrates during cognitive processes. Cereb Cortex Commun
678 3:tgac038.

679 Noto T, Zhou G, Schuele S, Templer J, Zelano C (2018) Automated analysis of breathing waveforms
680 using BreathMetrics. Chem Senses 43:583–597.

681 Park HD, Barnoud C, Trang H, Kannape OA, Schaller K, Blanke O (2020) Breathing is coupled with
682 voluntary action and the cortical readiness potential. Nat Commun 11:289.

683 Perl O, Ravia A, Rubinson M, Eisen A, Soroka T, Mor N, Secundo L, Sobel N (2019) Human non-
684 olfactory cognition phase-locked with inhalation. Nat Hum Behav 3:501–512.

685 Pfurtscheller G, Kaminski M, Blinowska KJ, Rassler B, Schwarz G, Klimesch W (2023) Respiration-
686 entrained brain oscillations in healthy fMRI participants with high anxiety. Sci Rep 13:2380.

687 R Core Team (2025) R: a language and environment for statistical computing. Vienna: R Foundation for
688 Statistical Computing.

689 Soroka T, Ravia A, Snitz K, Honigstein D, Weissbrod A, Gorodisky L, Weiss T, Perl O, Sobel N (2025)
690 Humans have nasal respiratory fingerprints. Curr Biol 35:3011–3021.e3.

691 Tort ABL, Brankačk J, Draguhn A (2018a) Respiration-entrained brain rhythms are global but often
692 overlooked. Trends Neurosci 41:186–197.

693 Tort ABL, Laplagne DA, Draguhn A, Gonzalez J (2025) Global coordination of brain activity by the
694 breathing cycle. Nat Rev Neurosci 26:333–353.

695 Tort ABL, Ponsel S, Jessberger J, Yanovsky Y, Brankačk J, Draguhn A (2018b) Parallel detection of theta
696 and respiration-coupled oscillations throughout the mouse brain. Sci Rep 8:6193.

697 Trimper JB, Stefanescu RA, Manns JR (2014) Recognition memory and theta-gamma interactions in the
698 hippocampus. Hippocampus 24:341–353.

699 Vasishth S, Nicenboim B, Beckman ME, Li F, Kong EJ (2018) Bayesian data analysis in the phonetic
700 sciences: a tutorial introduction. J Phonetics 71:147–161.

701 Virtanen P, Gommers R, Oliphant TE, Haberland M, Reddy T, Cournapeau D, Burovski E, Peterson P,
702 Weckesser W, Bright J, van der Walt SJ, Brett M, Wilson J, Millman KJ, Mayorov N, Nelson ARJ,
703 Jones E, Kern R, Larson E, et al. (2020) SciPy 1.0: fundamental algorithms for scientific computing
704 in Python. Nat Methods 17:261–272.

705 Vlemincx E, Van Diest I, Van den Bergh O (2015) Emotion, sighing, and respiratory variability.
706 Psychophysiology 52:657–666.

707 Watanabe T, Itagaki A, Hashizume A, Takahashi A, Ishizaka R, Ozaki I (2023) Observation of respiration-
708 entrained brain oscillations with scalp EEG. Neurosci Lett 797:137079.

709 Welch P (1967) The use of fast Fourier transform for the estimation of power spectra. IEEE Trans Audio
710 Electroacoust 15:70–73.

711 Zelano C, Jiang H, Zhou G, Arora N, Schuele S, Rosenow J, Gottfried JA (2016) Nasal respiration
712 entrains human limbic oscillations and modulates cognitive function. J Neurosci 36:12448–12467.

Zhou G, Olofsson JK, Koubeissi MZ, Menelaou G, Rosenow J, Schuele SU, Xu P, Voss JL, Lane G, Zelano C (2021) Human hippocampal connectivity is stronger in olfaction than other sensory systems. Prog Neurobiol 201:102027.

Figure Legends

Figure 1: Hypothesis and waveform shape quantification.

a. Quantification of respiration waveform shape. Airflow (top) and belt (bottom) signals shown with the following waveform features: rise time, decay time, area under the inhale peak, area under the exhale trough, inhale peak sharpness, and exhale trough sharpness. **b**. Overlay of individual respiratory cycles time-normalized to percentage of cycle, shown separately for airflow (top) and belt (bottom). Each colored trace represents an individual cycle; the dark overlaid line shows the cross-cycle mean. The spread of traces illustrates the heterogeneity of waveform morphology both within and across individuals and modalities. **c.** Simulated example illustrating the central hypothesis: a respiration signal (blue) with variable cycle morphology is shown alongside a simulated neural signal (yellow) whose waveform shape tracks that

of the respiration cycle-by-cycle. The central question of this paper is whether this waveform morphological coupling is observed in real intracranial EEG.

Figure 2: Data analysis pipeline.

a. Example airflow (top) and belt (bottom) traces from one participant. **b.** Power spectral density of airflow (top) and belt (bottom) signals fit via *specparam*, with the identified respiration peak frequency marked (green arrow). **c.** Three example neural channels (yellow) illustrating the sequential screening criteria for the example airflow channel (light blue). Coherence significance was assessed against 1,000 phase-randomized surrogate channels; CCF and PMI significance were assessed against permutation null distributions (1000 iterations each). Only channels passing all three criteria were retained for waveform shape analysis. For each channel (row), columns show the time series (airflow and neural), coherence, mean CCF, CCF null distribution, and PMI null distribution. Green outlines indicate the channel passed that criterion; red outlines indicate failure. Top row: a channel passing all screening criteria; significant coherence, CCF, and PMI exceeding the null. Middle row: a channel with significant coherence and CCF, but PMI failing time-domain screening. Bottom row: a channel failing coherence and all subsequent criteria. **d.** Extrema detection (top) and peak matching (bottom) on filtered and z-scored neural and respiratory signals. Matched peak pairs (red lines) defined the cycles used for feature extraction. **e.** Two example matched neural-respiratory cycle pairs with waveform shape features annotated: rise time (teal), decay time (red), inhale peak AUC (pink shading), exhale trough AUC (green shading), inhale peak sharpness (purple), and exhale trough sharpness (dark green). CCF, cross-correlation function; PMI, phase monotonicity index; AUC, area under curve.

Figure 3: Distribution of electrodes across brain regions showing respiration-brain coupling for airflow and belt signals.

a. Airflow-based coupling. Left: Percentage of total channels per region exhibiting significant coherence with nasal airflow (green). Right: Percentage of total channels per region showing significant respiration-

locked waveform shape (blue). **b.** Belt-based coupling. Left: Percentage of total channels per region exhibiting significant coherence with the respiratory belt signal (green). Right: Percentage of total channels per region showing significant respiration-locked waveform shape (blue). Numbers above bars represent raw counts of channels. Region-level overlap between airflow and belt coupling was Dice = 0.947 for coherence and Dice = 0.308 for waveform shape.

Figure 4: Respiratory waveform shape features are related to neural waveform shape features.

a. Posterior distributions of standardized slopes (β) from Bayesian linear mixed effects models relating respiratory features (rise time, decay time, cycle duration, rise-decay symmetry, inhale peak sharpness, exhale trough sharpness, inhale peak AUC, exhale trough AUC) to corresponding neural features. Slopes are standardized (z-scored predictors and outcomes), such that coefficients reflect effect sizes in SD units. Blue and purple distributions represent the posterior densities for airflow and belt, respectively. Gray distributions represent null model posteriors fit on data in which the within-subject respiratory predictor was shuffled across cycles to break cycle-by-cycle coupling. Positive values indicate that increases in respiratory feature magnitude are associated with increases in the corresponding neural feature. **b.** Posterior probability that each standardized slope is positive, $P(\beta > 0)$, for airflow and belt models. Darker shading indicates stronger evidence for a positive relationship. Airflow shows high posterior probability of positive slopes for cycle duration, decay time, and peak and trough AUC ($P(\beta > 0) \geq 0.99$), with moderate support for rise time and trough sharpness; null-model comparison indicates the AUC features are most robustly dissociated from cycle-shuffled data. Belt shows no directional evidence across features.

Figure 5: Cycle-by-cycle scatter plots of respiratory and neural waveform shape features.

Each point represents a single matched respiratory-neural cycle. Lines indicate within-channel regression fits; black lines indicate the overall regression fit across all channels and subjects. Airflow (blue) and belt (purple) modalities are shown separately for each feature pair: rise time, decay time, cycle duration, rise-decay symmetry, inhale peak sharpness, exhale trough sharpness, inhale peak AUC, and exhale trough

AUC. Positive slopes across participants are most consistent for airflow-derived temporal features (rise time, decay time, cycle duration) and amplitude-related features (inhale peak and exhale trough AUC), reflecting the within-subject coupling captured by the Bayesian models. Peak sharpness shows flat, variable slopes in both modalities. Trough sharpness shows a shallow but directionally positive slope for airflow. Belt regression lines are more inconsistent in direction across channels.

Tables

Table 1: Clinical and demographic information for all participants included in the study.

Participants were recruited from three sites: Northwestern University (participants 1–10), Children's National Hospital (participants 11–13) and the University of Iowa Stead Family Children's Hospital (participants 14–16). All participants were undergoing intracranial EEG monitoring for surgical evaluation of treatment-resistant epilepsy.

Participant	Site	Gender	Age at Surgery	Handedness	Duration of Epilepsy (years)	Epileptogenic Zone	Brain MRI
1	Northwestern	Male	32	Left	9	Left temporal lobe	Normal
2	Northwestern	Female	29	Right	7	Left temporal lobe	Normal
3	Northwestern	Male	49	Right	26	Left temporal lobe	Chronic stroke/encephalomalacia in left putamen, insula, parietal cortex
4	Northwestern	Male	48	R	11	Right temporal lobe	Normal
5	Northwestern	Male	32	Right	10	Left basal temporal	Normal
6	Northwestern	Female	27	Right	5	Left mesial temporal	Left mesial temporal sclerosis
7	Northwestern	Male	54	Left	2	Right mesial temporal	Normal

8	Northwestern	Female	25	Right	3	Left mesial temporal	Normal
9	Northwestern	Female	50	Right	27	Left temporal	Heterotopic gray matter to left atrial ependyma
10	Northwestern	Female	36	Right	4	Left frontal lobe	Possible moderate mesial temporal sclerosis
11	CNMC	Male	19	Right	18	Right temporal	Right amygdalohippocampectomy
12	CNMC	Female	19	Right	Unknown	Left temporal	Left amygdalectomy
13	CNMC	Male	21	Right	6	Focal, right frontal	Possible dysgenesis/dysplasis of right hippocampus
14	Iowa	Female	12	Right	8	Multifocal, but right mesial temporal preponderance	Normal
15	Iowa	Male	16	Right	9	Left anterior temporal lobe; mesial temporal lobe	Hypometabolism in the left media and anterior temporal lobe
16	Iowa	Female	14	Right	10	Right parieto-temporal region	Prior laser ablation of right posterior

							temporoparietal cortical dysplasia

Table 2: Electrode coverage.

Number of electrodes and participants contributing to each anatomical region for both the airflow and belt datasets.

	Airflow		Belt	
	No. of Electrodes	No. of Participants	No. of Electrodes	No. of Participants
Amygdala	37	11	46	12
Hippocampus	63	11	68	12
Entorhinal	3	2	3	2
Parahippocampal	9	4	8	4
Insula	86	10	66	10
Orbitofrontal cortex	53	7	61	8

Inferior frontal gyrus	62	10	49	10
Frontal–rostral middle	36	6	21	5
Frontal–caudal middle	25	5	24	4
Frontal–superior	36	5	30	3
Precentral	58	5	67	6
Paracentral	5	1	5	1
Postcentral	17	7	20	8
Cingulate cortex	33	4	35	4
Parietal–inferior	30	4	30	4
Parietal–superior	14	2	13	1
Occipital cortex	9	5	7	4
Fusiform	26	9	33	11
Temporal–middle	104	13	126	13
Temporal–inferior	36	11	50	12
Temporal–superior	88	12	93	13
Supramarginal	63	8	66	9
Transverse temporal	9	2	8	1
Thalamus	36	4	29	4

White matter	503	13	386	13
CSF	19	6	19	6
Total	1461	13	1363	13

810

811

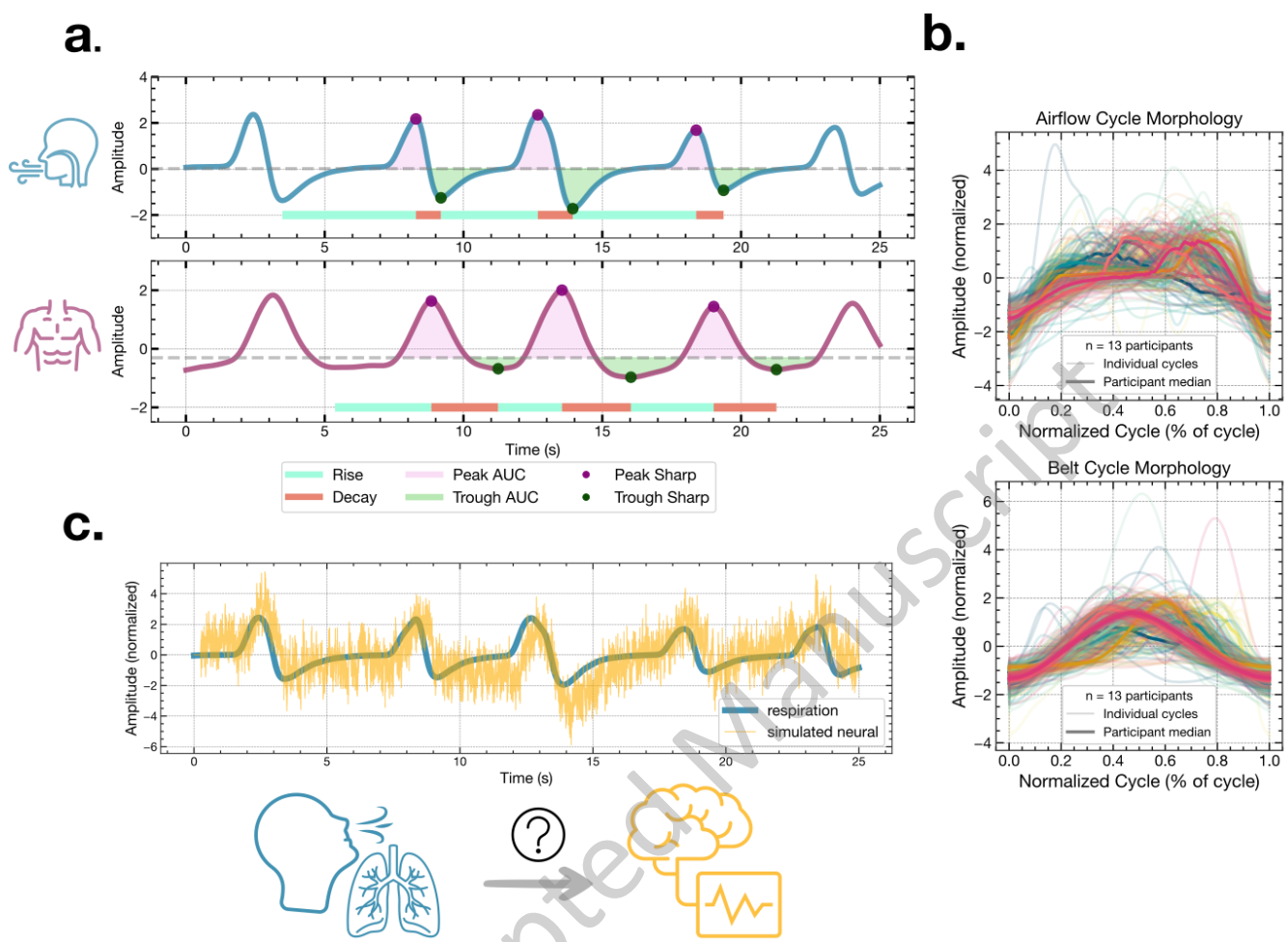

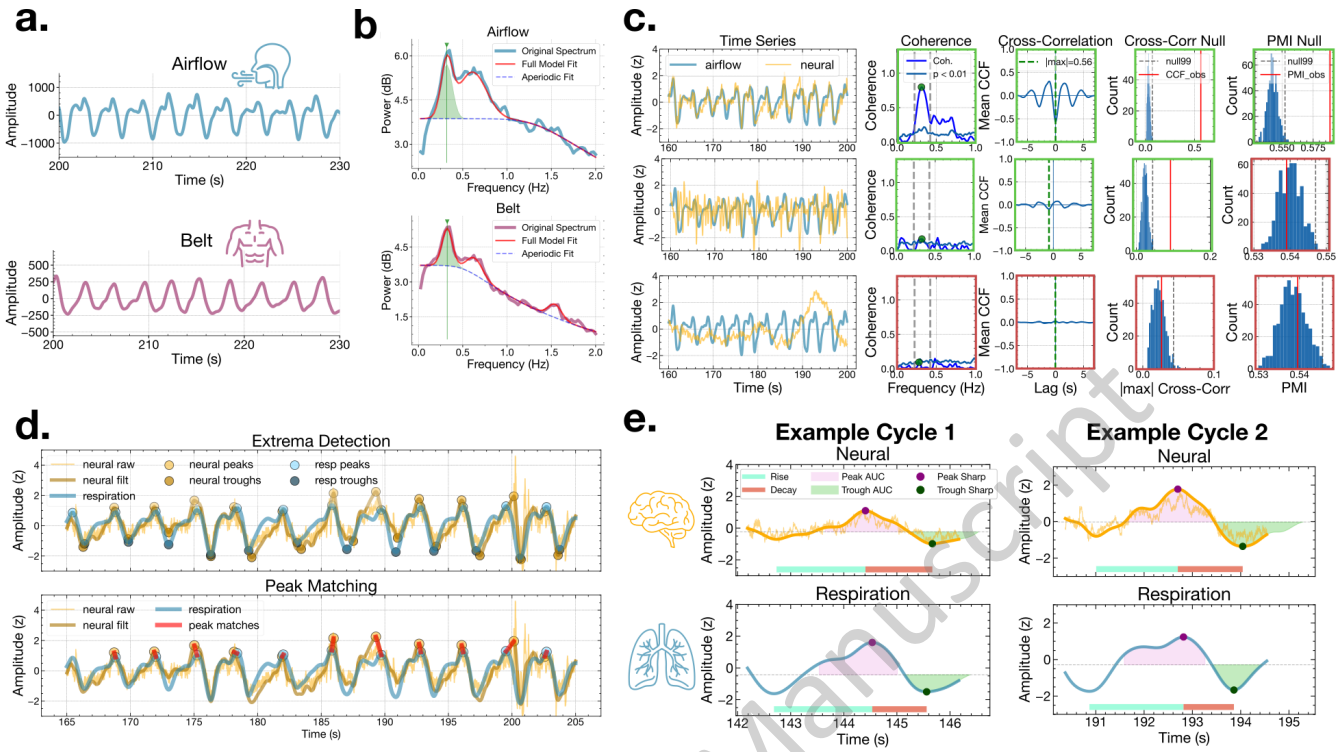

a.

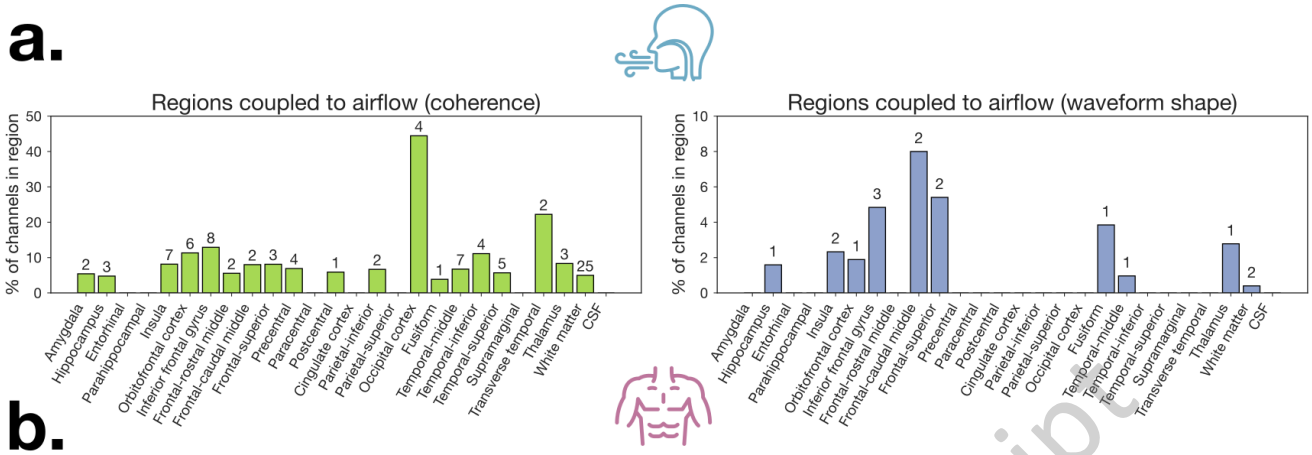

b.